

# Gate-Tunable Negative Longitudinal Magnetoresistance in the Predicted Type-II Weyl Semimetal $WTe_2$

Yaojia Wang<sup>1</sup>, Erfu Liu<sup>1</sup>, Huimei Liu<sup>1</sup>, Yiming Pan<sup>1</sup>, Longqiang Zhang<sup>1</sup>, Junwen Zeng<sup>1</sup>, Yajun Fu<sup>1</sup>, Miao Wang<sup>1</sup>, Kang Xu<sup>1</sup>, Zhong Huang<sup>1</sup>, Zhenlin Wang<sup>1</sup>, Haizhou Lu<sup>2</sup>, Dingyu Xing<sup>1</sup>, Baigeng Wang<sup>1\*</sup>, Xiangang Wan<sup>1\*</sup> & Feng Miao<sup>1\*</sup>

The progress in exploiting new electronic materials and devices has been a major driving force in solid-state physics. As a new state of matter, a Weyl semimetal (WSM), particularly a type-II WSM, hosts Weyl fermions as emergent quasiparticles and may harbor novel electrical transport properties because of the exotic Fermi surface. Nevertheless, such a type-II WSM material has not been experimentally observed in nature. In this work, by performing systematic magneto-transport studies on thin films of a predicted material candidate  $WTe_2$ , we observe notable angle-sensitive (between the electric and magnetic fields) negative longitudinal magnetoresistance (MR), which can likely be attributed to the chiral anomaly in WSM. This phenomenon also exhibits strong planar orientation dependence with the absence of negative longitudinal MR along the tungsten chains ( $a$  axis), which is consistent with the distinctive feature of a type-II WSM. By applying a gate voltage, we demonstrate that the Fermi energy can be tuned through the Weyl points via the electric field effect; this is the first report of controlling the unique transport properties *in situ* in a WSM system. Our results have important implications for investigating simulated quantum field theory in solid-state systems and may open opportunities for implementing new types of electronic applications, such as field-effect “chiral” electronic devices.

<sup>1</sup> National Laboratory of Solid State Microstructures, School of Physics, Collaborative Innovation Center of Advanced Microstructures, Nanjing University, Nanjing 210093, China.

<sup>2</sup> Department of Physics, South University of Science and Technology of China, Shenzhen, China.

Correspondence and requests for materials should be addressed to F. M. (email: [miao@nju.edu.cn](mailto:miao@nju.edu.cn)), X. W. (email: [xgwan@nju.edu.cn](mailto:xgwan@nju.edu.cn)), or B. W. (email: [bgwang@nju.edu.cn](mailto:bgwang@nju.edu.cn)).

Since the discovery of topological insulators, which significantly enriched band theory<sup>1,2</sup>, the possibility of realizing new topological states in materials other than insulators, such as semimetals or metals, has attracted substantial attention<sup>3-7</sup>. Weyl semimetals (WSMs), which host Weyl fermions<sup>8</sup> as emergent quasiparticles, have recently sparked intense research interest in condensed matter physics<sup>3,9-16</sup>. In WSMs, the conduction and valence bands linearly disperse across pairs of unremovable discrete points (Weyl points) along all three momentum directions<sup>3,17</sup>, with the existence of Fermi Arc surface states as a consequence of separated Weyl points with opposite chirality<sup>3</sup>. Since the first theoretical prediction in pyrochlore iridates<sup>3</sup>, several materials that break either the time-reversal or spatial-inversion symmetry have been proposed as WSMs, including a series of transition metal monophosphides<sup>12,13</sup>. These theoretical predictions have been experimentally confirmed by the observation of bulk Weyl points and surface Fermi Arcs<sup>18-21</sup>, or the signature of chiral anomaly<sup>15,22-30</sup> via electric transport studies. Many other new properties, such as the topological Hall effect<sup>14</sup> and non-local quantum oscillations<sup>31</sup>, have also been proposed.

The type-II WSM was recently proposed as a new type of WSM with Weyl points appearing at the boundary of electron and hole pockets<sup>32-35</sup>. Its distinctive feature of an open Fermi surface (in sharp contrast with a closed point-like Fermi surface in type-I WSMs) can induce exotic properties, such as planar orientation-dependent chiral anomaly. However, such type-II WSM materials have not been experimentally observed. As a unique layered transition-metal dichalcogenide (TMD) that exhibits large and unsaturated (perpendicular) magnetoresistance (MR)<sup>36</sup>, tungsten ditelluride (WTe<sub>2</sub>) has been reported as a major material candidate for type-II WSM. While angle-resolved photoemission spectroscopy (ARPES) measurements encounter certain challenges in observing the Weyl points because of the limited experimental spectroscopic resolution<sup>32,37</sup>, exploring the potential unique transport properties and realizing their tunability for future device applications are highly desirable.

In this report, low-temperature transport studies on thin WTe<sub>2</sub> samples are performed, revealing a clear negative longitudinal MR when the electric and magnetic fields are parallel. This phenomenon is highly angle sensitive and is suppressed by a

small angle between the electric and magnetic fields, and this behavior can likely be attributed to the chiral anomaly in the WSM. A unique property of type-II WSM, the planar orientation dependence, is also confirmed by the observed absence of negative longitudinal MR for all studied devices along the tungsten chains ( $\mathbf{a}$  axis). We further demonstrate that by applying a gate voltage, the Fermi energy of such a material can be effectively tuned through the Weyl points; thus, the unique transport properties can be controlled, suggesting possible applications in future “chiral” electronics.

WTe<sub>2</sub> is a T<sub>d</sub> type of TMD (space group  $Pnm2_1$ ) with a tungsten chain along the  $\mathbf{a}$  axis, as shown in Fig. 1a. The other principle axis, the  $\mathbf{b}$  axis, is perpendicular to the  $\mathbf{a}$  axis<sup>36,38</sup>. This T<sub>d</sub> phase breaks the inversion symmetry and was predicted to support the existence of type-II Weyl points<sup>32,33</sup>. We first focus on a key signature of the possibly existed Weyl points: the chiral-anomaly-induced negative longitudinal MR phenomenon. To make such observation feasible, thin flakes are required to sufficiently suppress the contribution of the strong positive longitudinal MR<sup>39</sup>. However, these thin flakes must be sufficiently “thick”, with energy bands similar to those of bulk crystals (see more details in the Supplementary Information) to permit the existence of Weyl points. Thus, we selected thin WTe<sub>2</sub> flakes with thicknesses of 7-15 nm, which were prepared using the standard mechanical exfoliation method on a SiO<sub>2</sub> substrate and measured using an atomic force microscope (AFM). The crystalline orientations were identified using polarized Raman spectra<sup>40</sup> (see more details in the Supplementary Information).

Thin WTe<sub>2</sub> devices with metal electrodes were fabricated using a home-made shadow mask method<sup>41</sup>, which effectively avoided undesirable wet process-induced doping in the pristine WTe<sub>2</sub> flakes<sup>42</sup>. A typical optical image of a four-probe device is shown in Fig. 1b, where the determined thickness of the thin flake was approximately 14 nm (inset of Fig. 1b). Fig. 1c shows the schematic drawing of the device structure and four-probe MR measurement setup. Here, the angle between the applied magnetic field  $\mathbf{B}$  and current direction  $\mathbf{I}$  is  $\theta$ .

To examine the possible signal of the chiral anomaly, we performed longitudinal MR measurements on the devices by applying a magnetic field (from -12 T to 12 T)

parallel or at small angles to the current direction at 1.6K. We observe two types of negative longitudinal MR phenomena when  $\mathbf{B} // \mathbf{I}$  ( $\theta=0^\circ$ ), with typical data shown in Figs. 2a (sample #1) and 2b (sample #2). Both types of negative longitudinal MR exhibit strong angle sensitivity with the strongest signal at  $\theta=0^\circ$  and an apparently suppressed signal at small  $\theta$  when the magnetic field was slightly rotated (pronounced suppression at approximately  $3^\circ$  and  $1.75^\circ$  for samples #1 and #2, respectively). Within a relatively small range of the magnetic field, weak anti-localization (WAL) effect was observed, and could be induced by the spin-orbit coupling in  $\text{WTe}_2$ <sup>43</sup>. Sample #1 shows only negative longitudinal MR at high magnetic field, and the magnetoresistance begins to decrease at approximately  $\pm 3.5$  T and continues over the entire studied magnetic field range (until  $\pm 12$  T). Sample #2 shows negative longitudinal MR with a positive MR signal at higher magnetic fields; the resistance begins to decrease at approximately  $\pm 1.1$  T, and the resistance subsequently increases from approximately  $\pm 4.7$  T. The observed positive longitudinal MR at higher magnetic fields is similar to what has been observed in  $\text{TaAs}$ <sup>26,27</sup> and  $\text{TaP}$ <sup>44,45</sup>. Its physical mechanism is still not clear, even though there are some theoretical proposals like the Coulomb interactions among the electrons occupying the chiral states<sup>26</sup> or the anisotropy of the Fermi surface<sup>46</sup>. In our thin-flake samples, the positive longitudinal MR is much suppressed compared to the reported value (1200%) in bulk crystals<sup>39</sup>, making the observation of the negative longitudinal MR feasible. To fully understand why the positive longitudinal MR gets suppressed for thinner samples is theoretically challenging at current stage and requires more future research efforts.

While the negative longitudinal MR is rare in non-ferromagnetic materials, it can serve as one of the key transport signatures in WSMs. Because the coupled Weyl points have opposite chiralities, the electrons are pumped from one point to the other and lead to a non-zero potential among them if the dot product of the magnetic and electric fields is not 0, i.e.,  $\mathbf{B} \cdot \mathbf{E} \neq 0$ . This chiral imbalance-induced potential will induce positive contribution to the conductance. Under the semi-classical approximation, when  $\mathbf{B} // \mathbf{E}$ , the anomaly conductivity<sup>23</sup> is described by

$$\sigma = \frac{e^4 v_F^3 \tau B^2}{4\pi^2 \hbar \Delta E^2} \quad (1)$$

where  $e$  is the electron charge,  $v_F$  is the Fermi velocity near the Weyl points,  $\Delta E$  is the measured chemical potential from the energy of the Weyl points, and  $\tau$  is the inter valley scattering time. The quadratic relation with a magnetic field leads to a negative MR effect with high sensitivity to the angle between  $\mathbf{B}$  and  $\mathbf{E}$ , which is consistent with our observations in thin WTe<sub>2</sub> samples.

There are few other origins other than the chiral anomaly, such as current-jetting<sup>47</sup> and magnetic effects<sup>48</sup>, could induce the negative longitudinal MR effect under certain conditions. Since WTe<sub>2</sub> is not a magnetic material, the possible origin of magnetic effects can be safely excluded. The current-jetting effect is usually induced by inhomogeneous currents generated when attaching point contact electrodes to a large bulk crystal. In our thin film devices (rather than bulk crystals) with well-defined electrodes, it can be excluded as well<sup>49</sup>. Several theoretic proposals related to defects or impurities are also not applicable in our systems. For example, the negative longitudinal MR observed in our samples is not as temperature-sensitive as the WAL effect (see more details in Supplementary Information), suggesting it is not related to the defects induced weak localization effect. Another theoretical work<sup>50,51</sup> predicting that certain impurities could induce negative longitudinal MR at small magnetic fields can be excluded, due to the fact that our observations happen at much higher fields (up to 12 T). In the case of ultra-quantum limit, the impurities were also suggested to induce negative longitudinal MR in any three-dimensional (3D) metal regardless of its band structures<sup>52</sup>. To investigate this prediction, by analyzing the measured Shubnikov-de Haas (SDH) oscillations (see more details in Supplementary Information), we carefully calculated the Landau level indexes of different samples exhibiting negative longitudinal MR. The results indicate that the samples remain in the semi-classical limit.

Thus, the negative longitudinal MR can be quantitatively analyzed using the formula<sup>27,53</sup> in the semi-classical limit, which includes the chiral anomaly contribution of the Weyl points:

$$\sigma_{xx}(B) = C_W B_{\parallel}^2 - C_{WAL} \left( \sqrt{B} \frac{B^2}{B^2 + B_c^2} + \gamma B^2 \frac{B_c^2}{B^2 + B_c^2} \right) + \sigma_0 \quad (2)$$

where  $C_W$  is the chiral coefficient,  $C_{WAL}$  is the WAL coefficient,  $B_c$  is the crossover critical field of two regions with different dependences (low field with  $B^2$  dependence and higher field with  $\sqrt{B}$  dependence)<sup>53</sup>, and  $\sigma_0$  is the zero field conductivity when  $\mathbf{B} \parallel \mathbf{I}$ . For small  $\theta$  values, the term of  $\sigma_0$  is replaced by  $\sigma_0/(1 + \mu^2 B_{\perp}^2)$  to represent the contribution of “transverse” positive MR, where  $\mu$  is the mobility. We analyzed the angle-dependent longitudinal MR data of sample #2 when  $0 \text{ T} < B < 3 \text{ T}$  and extracted the chiral coefficient  $C_W$  from the fitting results. The inset of Fig. 2c shows the fitting results of magneto-conductivity curves at various angles. The extracted  $C_W$  versus  $\theta$  data are plotted in Fig. 2c, revealing that  $C_W$  is an effective parameter characterizing the strength of the contribution from chiral anomaly, which exhibits strong longitudinal angle sensitivity.

A unique feature of the chiral anomaly in a type-II WSM is the predicted planar orientation dependence of the negative longitudinal MR effect due to the tilted band structure and coexistence of electron and hole pockets. We further examined the crystalline orientation dependence of the longitudinal MR along two principle axes. When the current was applied parallel to the  $\mathbf{b}$  axis (vertical to the tungsten chains), we observed negative longitudinal MR in all 4 measured samples (with aforementioned suitable thicknesses of 7-15 nm) (see more details in the Supplementary Information). In sharp contrast, for all 4 studied samples under similar conditions (exfoliated from the same batch of single crystals and in the identical thickness range) but different current orientation parallel to the  $\mathbf{a}$  axis (the tungsten chains), only positive longitudinal MR was observed (see more details in the Supplementary Information). These findings support the predicted signature of the type-II Weyl fermion chiral anomaly in thin  $\text{WTe}_2$  films<sup>32</sup> (see more details in Supplementary Information).

Compared to other experimentally studied WSMs (all bulk materials with fixed doping), another enormous advantage of a thin-layered type-II WSM is the potential for realizing gate tunability, which lies at the heart of modern electronics, and more importantly, is crucial to verify the negative longitudinal MR as a signature of topological semimetal. The negative longitudinal MR in topological semimetals arises from their “monopoles” in momentum space, which generate a nontrivial Berry

curvature that couples an external magnetic field to the velocity of electrons. As a result, an extra chiral current can be induced in parallel magnetic fields, leading to the negative MR. Because the Berry curvature diverges at the Weyl nodes<sup>23,25</sup>, the negative longitudinal MR is expected to be maximized at the Weyl nodes. Therefore, to verify the negative longitudinal MR as a signature of topological semimetal, it is crucial to measure its dependence on the carrier density with a tunable gate voltage *in situ*. So far, no such experiment has been reported in WSMs.

Gate-tunable negative longitudinal MR effect in WTe<sub>2</sub> thin films has been observed in most studied devices. Fig. 3a shows the longitudinal MR of sample #1 for various back gate voltages  $V_{bg}$  from -40 V to 40 V. While the negative longitudinal MR was pronounced at -40 V, it was gradually suppressed as  $V_{bg}$  increased and was nearly completely suppressed at 40 V, as indicated by the extracted  $C_w$  plot in Fig. 3b (see fitting curves presented in Supplementary Information). This result implies that as  $V_{bg}$  increases, the Fermi energy increases and moves away from the Weyl points from above. In contrast, an opposite trend (monotonously increasing  $C_w$  with increasing  $V_{bg}$ ) was observed in sample #3 (as shown in the inset of Fig. 3b; see more details in the Supplementary Information), suggesting that the Fermi energy approaches the Weyl points from below.

More interestingly, a non-monotonous  $C_w$ - $V_{bg}$  curve is observed in sample #2 with  $C_w$  maximized at certain  $V_{bg}$ . As shown in Fig. 3c, as  $V_{bg}$  increases from -40 V to 0 V, the native longitudinal MR is gradually enhanced until reaching a maximum between 0 V and 20 V. When higher  $V_{bg}$  is applied, the native longitudinal MR is apparently suppressed. The  $C_w$  data extracted from the complete dataset are plotted in Fig. 3d, showing the maximum value of  $C_w$  in the range of 10-17.5 V. Because the anomaly conductivity reaches the maximum while crossing the Weyl points, these results indicate that we can successfully access the Weyl points via gate tuning. While modulating other bulk WSMs is mostly achieved through chemical/physical doping approaches, and the material properties are fixed by the selected composition and doping level during material processing, the *in-situ* tuning of the Fermi energy in layered type-II WSMs could provide an important platform to explore “Chiral” physics



of type-II Weyl fermions.

In conclusion, our observations of the angle-sensitive negative longitudinal MR and the strong planar orientation dependence in thin WTe<sub>2</sub> samples reveal important signatures of chiral anomaly in such a predicted type-II WSM. Taking advantage of the thin-film geometry, we successfully demonstrated the *in-situ* tuning of the Fermi energy through the Weyl points, resolving the tunability of unique transport properties and verifying the negative longitudinal MR as a signature of topological semimetal. Our results suggest that gated thin WTe<sub>2</sub> films may constitute a new and ideal platform to control and exploit the unique properties of type-II Weyl fermions (around the Weyl points) using numerous experimental techniques and pave the way for the implementation of future “chiral” electronics.

## Methods

The WTe<sub>2</sub> thin films were mechanical exfoliated from single crystals (HQ-graphene, Inc.) onto the silicon substrate covered by 285 nm SiO<sub>2</sub>. The thickness of the samples was confirmed by using a Bruker Multimode 8 Atomic Force Microscopy (AFM). The electrodes (5 nm Ag/40 nm Au) were patterned using home-made shadow mask method and deposited by standard electron beam evaporation. The devices were measured in an Oxford cryostat with a magnetic field of up to 12 T and based temperature of about 1.6 K. The MR signals were collected by using a low frequency Lock-in amplifier.

In our experiments, we used a rotary insert (Oxford Instruments) to tilt the angle between the magnetic field and current,  $\theta$ . While the magnitude and direction of the magnetic field is fixed, rotating a device placed on the rotation unit is equivalent to rotating the magnetic field with a fixed device current direction. The rotary insert has precise control on the tilted angle, with error only about  $\pm 0.05^\circ$ .

## References:

1. Hasan, M. Z. & Kane, C. L., Colloquium: Topological insulators. *Rev. Mod. Phys.* **82**, 3045-3067 (2010).

2. Qi, X. L. & Zhang, S. C., Topological insulators and superconductors. *Rev. Mod. Phys.* **83**, 1057 (2011).
3. Wan, X. G., Turner, A. M., Vishwanath, A. & Savrasov, S. Y., Topological semimetal and Fermi-arc surface states in the electronic structure of pyrochlore iridates. *Phys. Rev. B* **83**, 205101 (2011).
4. Balents, L., Weyl electrons kiss. *Physics* **4**, 36 (2011).
5. Young, S. M. *et al.*, Dirac Semimetal in Three Dimensions. *Phys. Rev. Lett.* **108**, 140405 (2012).
6. Wang, Z. J. *et al.*, Dirac semimetal and topological phase transitions in  $A_3Bi$  ( $A = Na, K, Rb$ ). *Phys. Rev. B* **85**, 195320 (2012).
7. Wang, Z. J., Weng, H. M., Wu, Q. S., Dai, X. & Fang, Z., Three-dimensional Dirac semimetal and quantum transport in  $Cd_3As_2$ . *Phys. Rev. B* **88**, 125427 (2013).
8. Weyl, H., Elektron und Gravitation. I. *Zeitschrift für Physik* **56**, 330-352 (1929).
9. Xu, G., Weng, H. M., Wang, Z. J., Dai, X. & Fang, Z., Chern Semimetal and the Quantized Anomalous Hall Effect in  $HgCr_2Se_4$ . *Phys. Rev. Lett.* **107**, 186806 (2011).
10. Burkov, A. A. & Balents, L., Weyl Semimetal in a Topological Insulator Multilayer. *Phys. Rev. Lett.* **107**, 127205 (2011).
11. Halasz, G. B. & Balents, L., Time-reversal invariant realization of the Weyl semimetal phase. *Phys. Rev. B* **85**, 035103 (2012).
12. Weng, H. M., Fang, C., Fang, Z., Bernevig, B. A. & Dai, X., Weyl Semimetal Phase in Noncentrosymmetric Transition-Metal Monophosphides. *Phys. Rev. X* **5**, 011029 (2015).
13. Huang, S. M. *et al.*, A Weyl Fermion semimetal with surface Fermi arcs in the transition metal monpnictide TaAs class. *Nat. Commun.* **6**, 7373 (2015).
14. Yang, K. Y., Lu, Y. M. & Ran, Y., Quantum Hall effects in a Weyl semimetal: Possible application in pyrochlore iridates. *Phys. Rev. B* **84**, 075129 (2011).
15. Kim, H. *et al.*, Dirac versus Weyl Fermions in Topological Insulators: Adler-Bell-Jackiw Anomaly in Transport Phenomena. *Phys. Rev. Lett.* **111**, 246603 (2013).
16. Hosur, P. & Qi, X., Recent developments in transport phenomena in Weyl semimetals. *Comp. Rend. Phys.* **14**, 857-870 (2013).
17. Murakami, S., Phase transition between the quantum spin Hall and insulator phases in 3D: emergence of a topological gapless phase. *New J. Phys.* **9**, 356 (2007).
18. Xu, S. Y. *et al.*, Discovery of a Weyl fermion semimetal and topological Fermi arcs. *Science* **349**, 613-617 (2015).
19. Lv, B. Q. *et al.*, Experimental Discovery of Weyl Semimetal TaAs. *Phys. Rev. X* **5**, 031013 (2015).
20. Lv, B. Q. *et al.*, Observation of Weyl nodes in TaAs. *Nat. Phys.* **11**, 724-727 (2015).
21. Yang, L. X. *et al.*, Weyl semimetal phase in the non-centrosymmetric compound TaAs. *Nat. Phys.* **11**, 728-732 (2015).
22. Nielsen, H. B. & Ninomiya, M., The Adler-Bell-Jackiw anomaly and Weyl fermions in a crystal. *Phys. Lett. B* **130**, 389-396 (1983).
23. Son, D. T. & Spivak, B. Z., Chiral anomaly and classical negative magnetoresistance of Weyl metals. *Phys. Rev. B* **88**, 104412 (2013).
24. Aji, V., Adler-Bell-Jackiw anomaly in Weyl semimetals: Application to pyrochlore iridates. *Phys. Rev. B* **85**, 241101 (2012).
25. Burkov, A. A., Negative longitudinal magnetoresistance in Dirac and Weyl metals. *Phys. Rev. B* **91**, 245157 (2015).
26. Huang, X. *et al.*, Observation of the Chiral-Anomaly-Induced Negative Magnetoresistance in 3D

- Weyl Semimetal TaAs. *Phys. Rev. X* **5**, 031023 (2015).
27. Zhang, C. L. *et al.*, Signatures of the Adler - Bell - Jackiw chiral anomaly in a Weyl fermion semimetal. *Nat. Commun.* **7**, 10735 (2016).
  28. Xiong, J. *et al.*, Evidence for the chiral anomaly in the Dirac semimetal Na<sub>3</sub>Bi. *Science* **350**, 413-416 (2015).
  29. Li, H. *et al.*, Negative magnetoresistance in Dirac semimetal Cd<sub>3</sub>As<sub>2</sub>. *Nat. Commun.* **7**, 10301 (2016).
  30. Li, C. *et al.*, Giant negative magnetoresistance induced by the chiral anomaly in individual Cd<sub>3</sub>As<sub>2</sub> nanowires. *Nat. Commun.* **6**, 10137 (2015).
  31. Potter, A. C., Kimchi, I. & Vishwanath, A., Quantum oscillations from surface Fermi arcs in Weyl and Dirac semimetals. *Nat. Commun.* **5**, 5161 (2014).
  32. Soluyanov, A. A. *et al.*, Type-II Weyl semimetals. *Nature* **527**, 495-498 (2015).
  33. Sun, Y., Wu, S. C., Ali, M. N., Felser, C. & Yan, B. H., Prediction of Weyl semimetal in orthorhombic MoTe<sub>2</sub>. *Phys. Rev. B* **92**, 161107 (2015).
  34. Chang, T. R. *et al.*, Prediction of an arc-tunable Weyl Fermion metallic state in Mo<sub>x</sub>W<sub>1-x</sub>Te<sub>2</sub>. *Nat. Commun.* **7**, 10639 (2016).
  35. Koepf, K. *et al.*, TaIrTe<sub>4</sub> a ternary Type-II Weyl semi-metal. <http://arXiv.org/abs/1603.04323> (2016).
  36. Ali, M. N. *et al.*, Large, non-saturating magnetoresistance in WTe<sub>2</sub>. *Nature* **514**, 205-208 (2014).
  37. Belopolski, I. *et al.*, Unoccupied electronic structure and signatures of topological Fermi arcs in the Weyl semimetal candidate Mo<sub>x</sub>W<sub>1-x</sub>Te<sub>2</sub>. <http://arXiv.org/abs/1512.09099> (2015).
  38. Augustin, J. *et al.*, Electronic band structure of the layered compound Td-WTe<sub>2</sub>. *Phys. Rev. B* **62**, 10812-10823 (2000).
  39. Zhao, Y. F. *et al.*, Anisotropic magnetotransport and exotic longitudinal linear magnetoresistance in WTe<sub>2</sub> crystals. *Phys. Rev. B* **92**, 041104 (2015).
  40. Kong, W. D. *et al.*, Raman scattering investigation of large positive magnetoresistance material WTe<sub>2</sub>. *Appl. Phys. Lett.* **106**, 081906 (2015).
  41. Bao, W. Z. *et al.*, Lithography-free fabrication of high quality substrate-supported and freestanding graphene devices. *Nano Res.* **3**, 98-102 (2010).
  42. Vieu, C. *et al.*, Electron beam lithography: resolution limits and applications. *Appl. Surf. Sci.* **164**, 111-117 (2000).
  43. Wang, L. *et al.*, Tuning magnetotransport in a compensated semimetal at the atomic scale. *Nat. Commun.* **6**, 8892 (2015).
  44. Du, J. *et al.*, Unsaturated both large positive and negative magnetoresistance in Weyl Semimetal TaP. <http://arXiv.org/abs/1507.05246> (2015).
  45. Arnold, F. *et al.*, Large and unsaturated negative magnetoresistance induced by the chiral anomaly in the Weyl semimetal TaP. <http://arXiv.org/abs/1506.06577> (2015).
  46. Pal, H. K. & Maslov, D. L., Necessary and sufficient condition for longitudinal magnetoresistance. *Phys. Rev. B* **81**, 214438 (2010).
  47. Hu, J. S., Rosenbaum, T. F. & Betts, J. B., Current jets, disorder, and linear magnetoresistance in the silver chalcogenides. *Phys. Rev. Lett.* **95**, 186603 (2005).
  48. Ritchie, L. *et al.*, Magnetic, structural, and transport properties of the Heusler alloys Co<sub>2</sub>MnSi and

NiMnSb. *Phys. Rev. B* **68**, 104430 (2003).

49. R. D. Dos Reis *et al.*, On the search for the chiral anomaly in Weyl semimetals: The negative longitudinal magnetoresistance. <http://arXiv.org/abs/1606.03389> (2016).

50. Zhang, S. B., Lu, H. Z. & Shen, S. Q., Chiral anomaly and linear magnetoconductivity in a topological Weyl semimetal. <http://arXiv.org/abs/1509.02001> (2016).

51. Goswami, P., Pixley, J. H. & Das Sarma, S., Axial anomaly and longitudinal magnetoresistance of a generic three-dimensional metal. *Phys. Rev. B* **92**, 075205 (2015).

52. Argyres, P. N. & Adams, E. N., Longitudinal Magnetoresistance in the Quantum Limit. *Phys. Rev* **104**, 900-908 (1956).

53. Lu, H. Z. & Shen, S. Q., Weak antilocalization and localization in disordered and interacting Weyl semimetals. *Phys. Rev. B* **92**, 035203 (2015).

## **Acknowledgements**

This work was supported in part by the National Key Basic Research Program of China (2015CB921600, 2013CBA01603 and 2016YFA0301703), National Natural Science Foundation of China (11374142, 61574076, 11525417, 11374137 and 11574127), Natural Science Foundation of Jiangsu Province (BK20130544, BK20140017, and BK20150055), Specialized Research Fund for the Doctoral Program of Higher Education (20130091120040), China Postdoctoral Science Foundation, Fundamental Research Funds for the Central Universities, and Collaborative Innovation Center of Advanced Microstructures.

## **Author contributions**

F. M. and Y. W. conceived the project and designed the experiments. Y. W., E. L., J. Z., Y. F., M. W. and K. X. performed the device fabrication and electrical measurements. Y. W., F. M., X. W., H. Lu, B. W., E. L., H. Liu, Y. P. and L. Z. conducted the data analysis and interpretation. Y. W., E. L., Z. H. and Z. W. carried out the Raman spectroscopy measurements and analysis. F. M., X. W., Y. W. and H. Lu co-wrote the paper, and all authors contributed to discussions about and the preparation of the manuscript.

## **Competing financial interests**

The authors declare no competing interests.

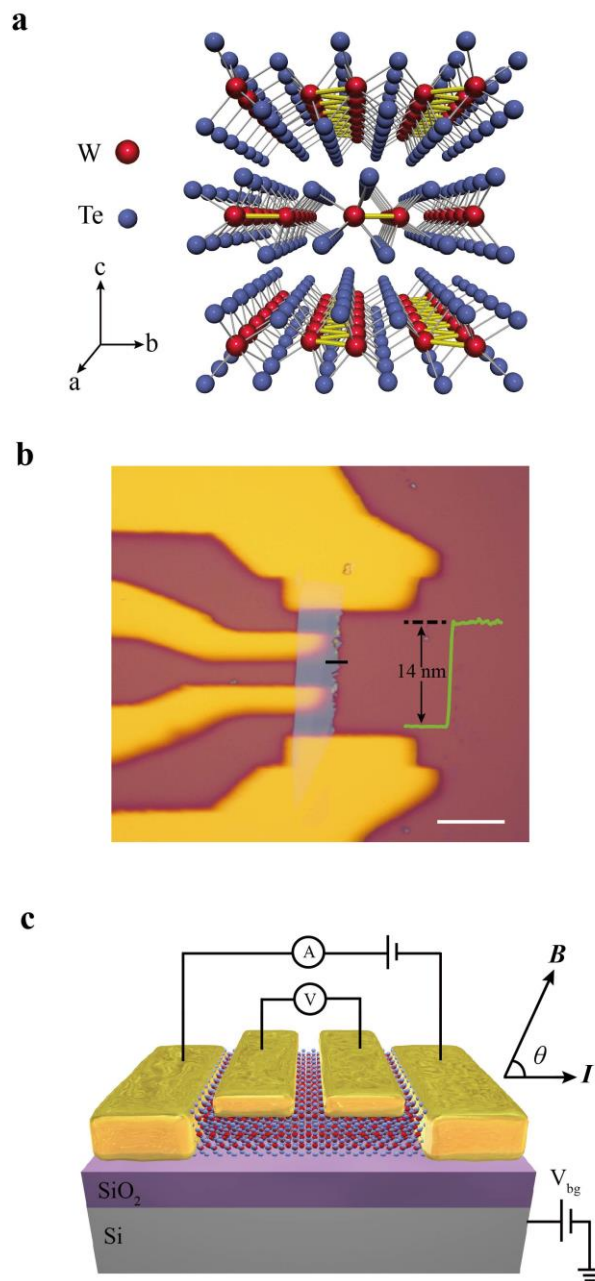


**Figure 1 | Thin WTe<sub>2</sub> film devices.** **a**, The crystal structure of WTe<sub>2</sub>; the yellow zigzag lines represent the tungsten chains along the *a* axis. **b**, Optical image of a four-probe thin WTe<sub>2</sub> film device. Scale bar: 15 μm. Inset: AFM height profile of the flake along the black line. **c**, Schematic structure and measurement circuit of the gated four-probe devices. The angle between the magnetic field and current is defined as  $\theta$ .

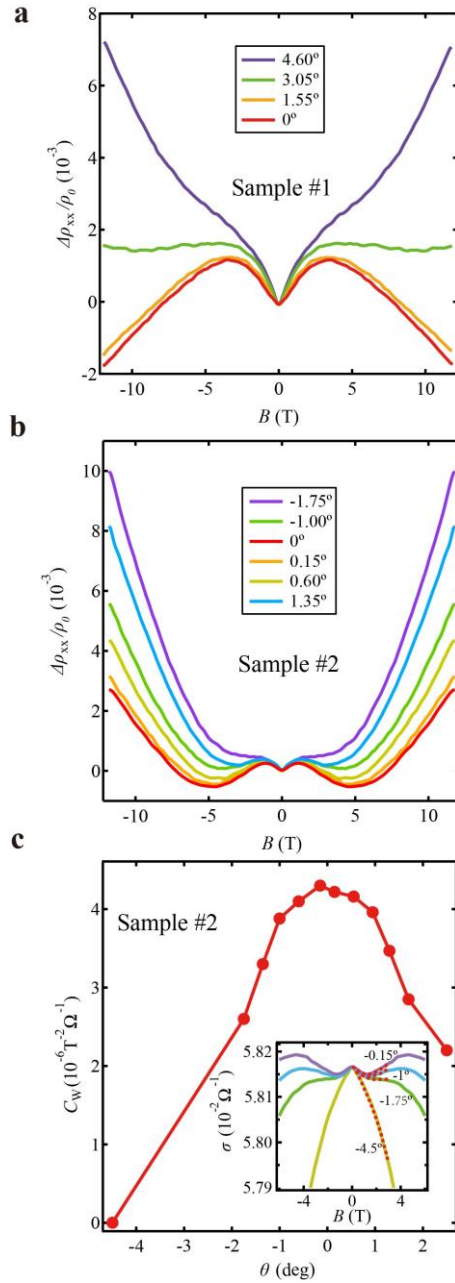


**Figure 2 | Angle-dependent negative longitudinal MR of thin WTe<sub>2</sub>.** **a**, Sample #1 exhibits only negative longitudinal MR at high magnetic fields, which is apparently suppressed at approximately 3°. **b**, Sample #2 exhibits a negative longitudinal MR and a positive MR signal at higher magnetic field, which is apparently suppressed at approximately 1.75°. **c**, The extracted chiral anomaly coefficient  $C_W$  for sample #2 was obtained from fittings with the semi-classical formula. The results show strong angle  $\theta$  sensitivity. Inset: fitting result (red dashed lines) of experimental magnetoconductivity curves (solid lines) at various angles. The MR data were collected at 1.6 K.

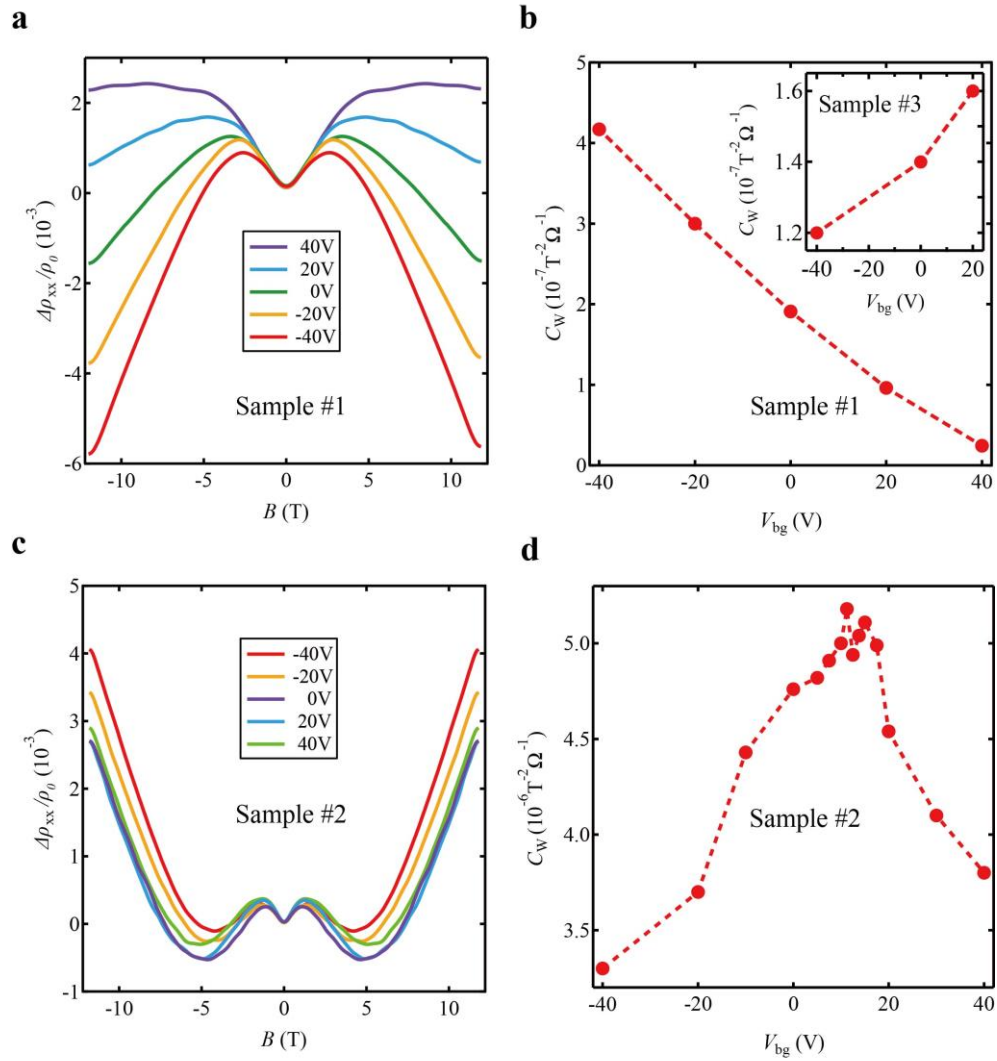


**Figure 3| Gate-tunable negative longitudinal MR of thin WTe<sub>2</sub>.** **a**, The negative longitudinal MR of sample #1 for various  $V_{bg}$ , which shows a suppressed negative longitudinal MR effect with increasing  $V_{bg}$  from +40 V to -40 V. **b**, Plot of the extracted chiral anomaly coefficient  $C_w$  of samples #1 (main) and #3 (inset), showing monotonous decreased/increased  $C_w$  with increasing  $V_{bg}$ . **c**, The negative longitudinal MR of sample #2 for various  $V_{bg}$  shows a non-monotonous  $C_w$ - $V_{bg}$  dependence with a maximum  $C_w$  at certain  $V_{bg}$ . **d**, The  $C_w$  data extracted from the complete dataset are partially shown in Fig. 3d, where the maximum value of  $C_w$  occurs at 10-17.5 V.

## Supplementary Information

### Gate-Tunable Negative Longitudinal Magnetoresistance in the Predicted Type-II Weyl Semimetal $WTe_2$

Yaojia Wang<sup>1</sup>, Erfu Liu<sup>1</sup>, Huimei Liu<sup>1</sup>, Yiming Pan<sup>1</sup>, Longqiang Zhang<sup>1</sup>, Junwen Zeng<sup>1</sup>, Yajun Fu<sup>1</sup>, Miao Wang<sup>1</sup>, Kang Xu<sup>1</sup>, Zhong Huang<sup>1</sup>, Zhenlin Wang<sup>1</sup>, Haizhou Lu<sup>2</sup>, Dingyu Xing<sup>1</sup>, Baigeng Wang<sup>1\*</sup>, Xiangang Wan<sup>1\*</sup> & Feng Miao<sup>1\*</sup>

*1 National Laboratory of Solid State Microstructures, School of Physics, Collaborative Innovation Center of Advanced Microstructures, Nanjing University, Nanjing 210093, China.*

*2 Department of Physics, South University of Science and Technology of China, Shenzhen, China.*

Correspondence and requests for materials should be addressed to F. M. (email: [miao@nju.edu.cn](mailto:miao@nju.edu.cn)), X. W. (email: [xgwan@nju.edu.cn](mailto:xgwan@nju.edu.cn)), or B. W. (email: [bgwang@nju.edu.cn](mailto:bgwang@nju.edu.cn)).



## 1. Layer number dependence of the energy band

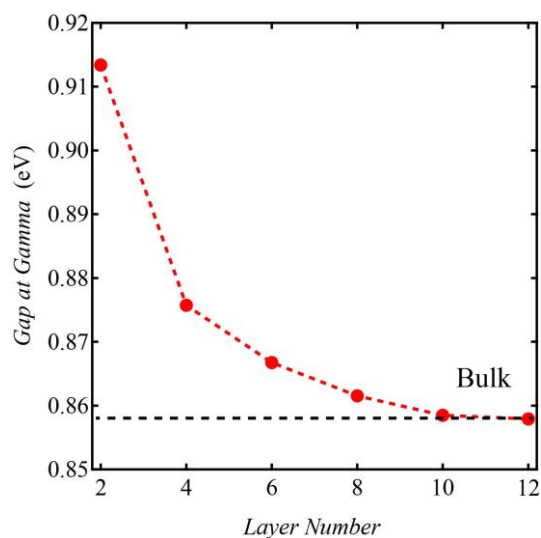
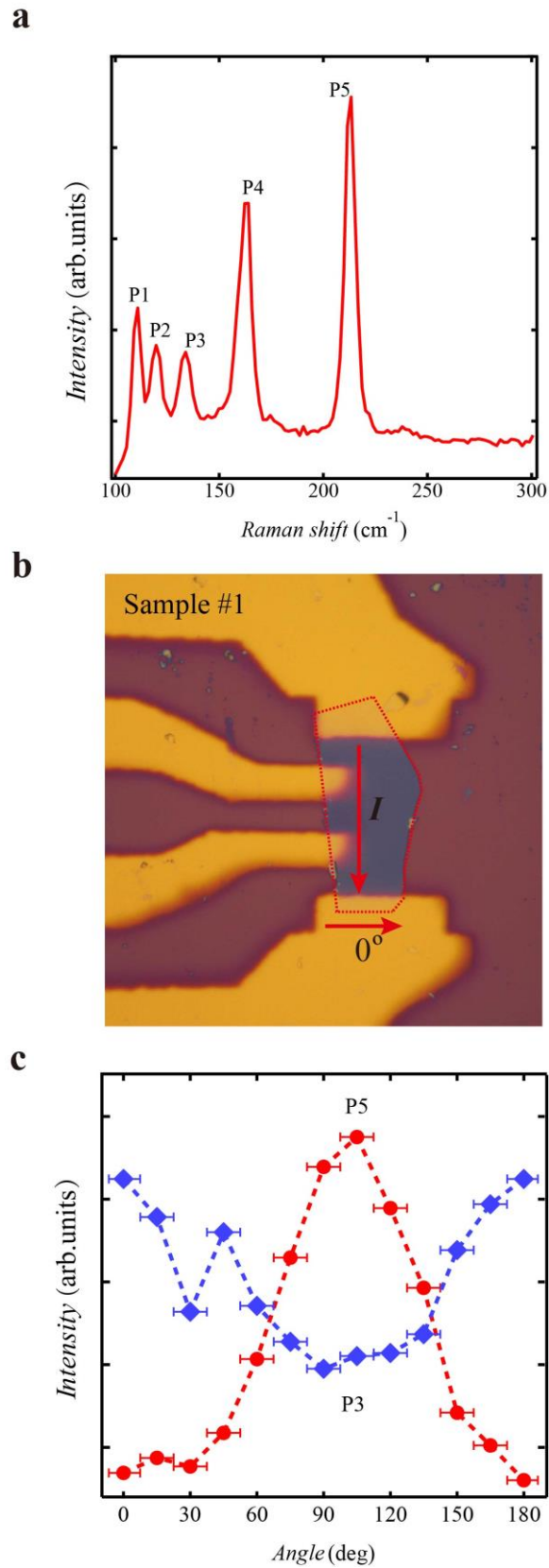


**Figure S1 | Layer number dependence of the band gap at  $\Gamma$  (0, 0, 0) point of WTe<sub>2</sub>.**

The energy bands of layered materials are generally sensitive to the thickness (layer number) when approaching 2D. Because Weyl fermions cannot exist in a 2D system, to explore the lower band thickness appropriate for our studies, we calculated the gap at  $\Gamma$  (0, 0, 0) of the Brillouin Zone of WTe<sub>2</sub> with different layer numbers. A vacuum spacing of 15 Å was used so that the interaction in the non-periodic directions could be neglected. As shown in Fig. S1, the band gap at  $\Gamma$  point is sensitive to the layer number and tends to be constant when the layer number approaches 10 (approximately 7 nm), suggesting that the films thicker than 7 nm share energy bands similar to those of the bulk samples, permitting the existence of Weyl points. This result is consistent with our experimental observation that the negative longitudinal MR effect is only observed in the 7-15-mm-thick samples and not in samples thinner than 7 nm.

## 2. Raman scattering measurements

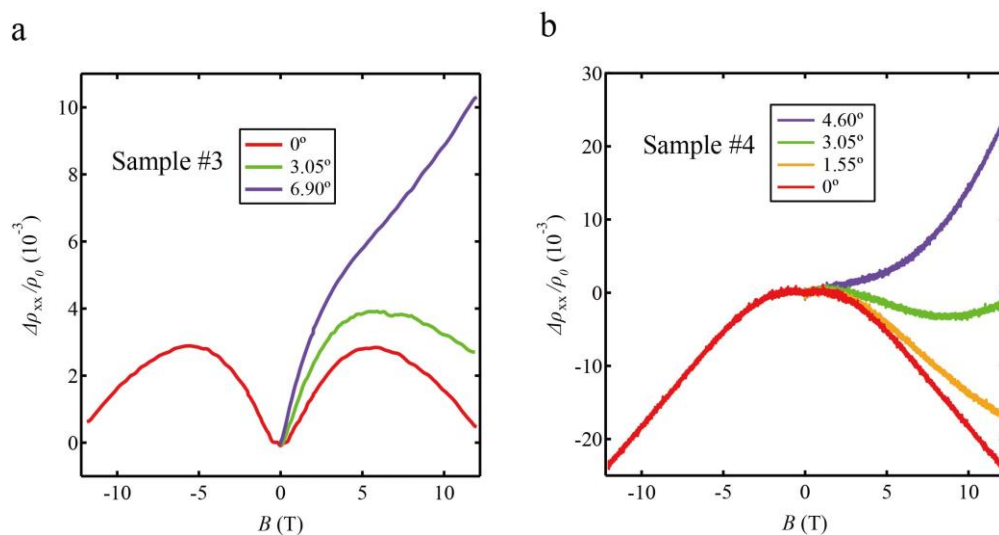
The polarized Raman scattering spectra were used to determine the crystal orientation of thin WTe<sub>2</sub> samples. The measurements were performed using a 514-nm excitation laser at room temperature. Here, we show the measurement results of sample #1 as an example. The non-polarized Raman spectra are shown in Fig. S2a, where five peaks are detected at 110.8 cm<sup>-1</sup> (P1), 119.7 cm<sup>-1</sup> (P2), 133.9 cm<sup>-1</sup> (P3), 164 cm<sup>-1</sup> (P4), and 213.3 cm<sup>-1</sup> (P5), similar to the reported results<sup>1</sup>. When the incident polarization vector ( $e_i$ ) is parallel to the scattered polarization vector ( $e_s$ ), the angle dependence of the intensities of P3 and P5 exhibits a two-fold symmetry with a phase difference of 90°<sup>1</sup>. According to Ref (1), the intensities of P3 and P5 are maximized and minimized, respectively, when  $e_i$  and  $e_s$  are parallel to the  $a$  axis. As shown in Fig. S2c, the intensities of P3 and P5 approach the maximum values near 0° and 90° respectively, where the angle definition is shown in the device image in Fig. S2b. The measurement error for the angles is approximately  $\pm 7.5^\circ$ . Based on these results, we determine that 0° is along the  $a$  axis and that the current direction is along the  $b$  axis.



**Figure S2 | Polarized Raman scattering spectra of sample #1. a.** Non-polarized Raman scattering spectra. **b.** Device picture with angle definition as marked by the red arrows. The dashed red lines indicate the shape of the flake. **c.** Angle dependence of the

intensities of P3 and P5.

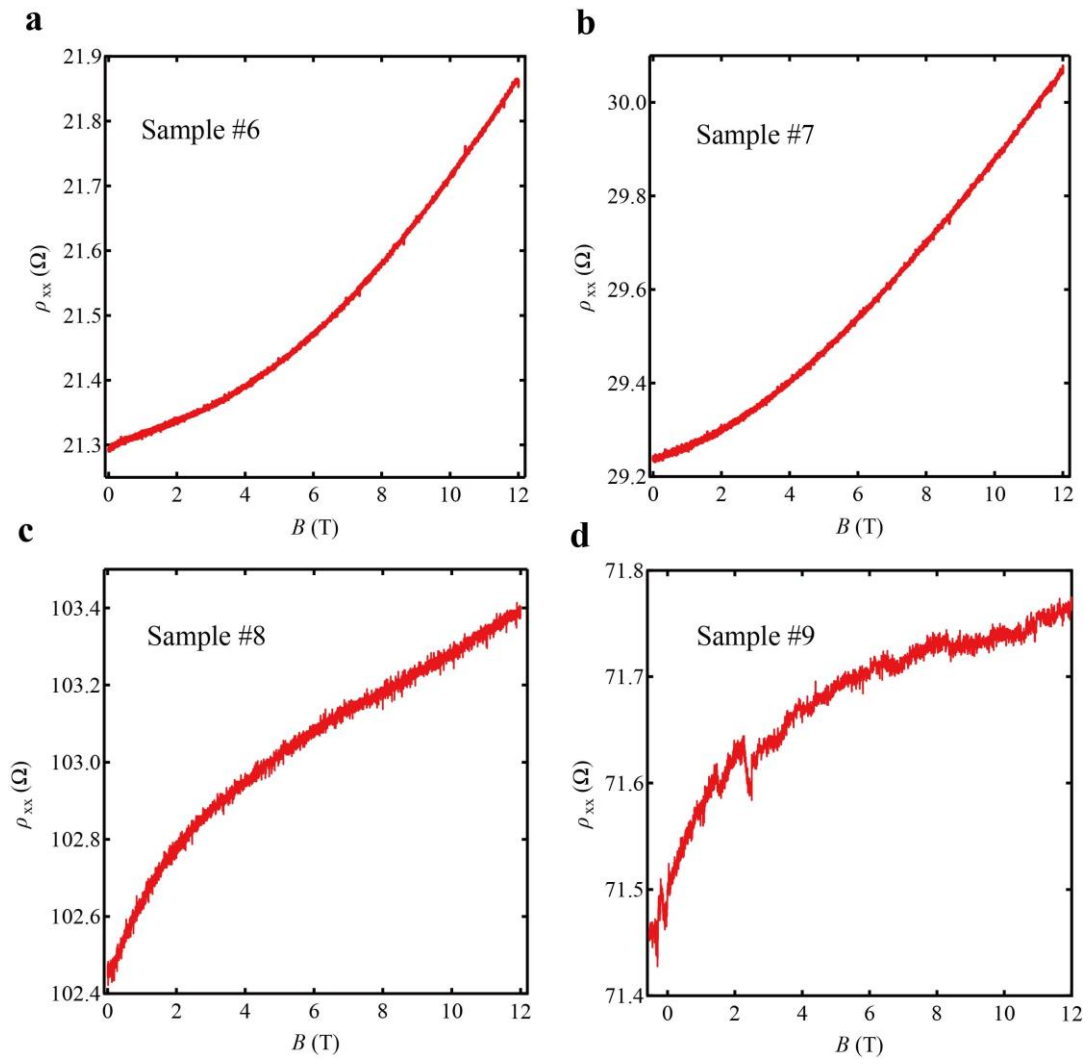
### 3. Additional data for the angle-dependent negative longitudinal MR with $I//b$



**Figure S3 | Angle-dependent negative longitudinal MR of additional samples.** **a.** and **b.** show the datasets of samples #3 and #4, respectively. Both samples were measured with current along the  $b$  axis and exhibit strong angle  $\theta$  sensitivity.

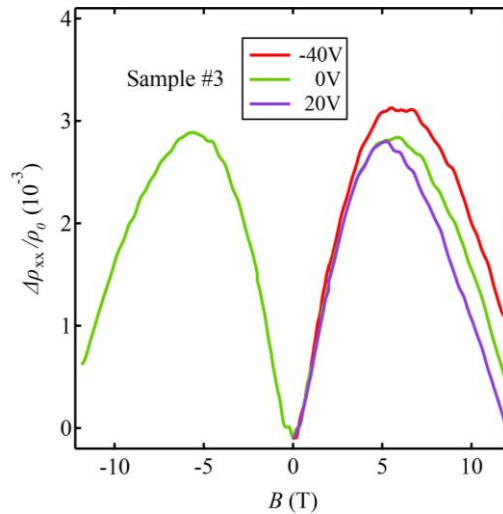
### 4. MR of all measured samples with current along the $a$ axis

A key feature of the chiral anomaly in a type-II WSM is the predicted planar orientation dependence of the negative longitudinal MR effect<sup>2</sup>. As a predicted type-II WSM, the calculation results of WTe<sub>2</sub> suggest the absence of the chiral anomaly along the direction of the  $a$  axis (the tungsten chains). We study 4 samples with current applied along the  $a$  axis. These samples were prepared under very similar conditions (exfoliated from the same batch of single crystals and within the thickness range of 7-15 nm). As shown in Fig. S4, only positive longitudinal MR is observed in all 4 samples, supporting the predicted planar orientation dependence of the type-II Weyl fermion chiral anomaly in thin WTe<sub>2</sub> films.



**Figure S4 | Longitudinal MR of all measured samples with current along the  $a$  axis.**

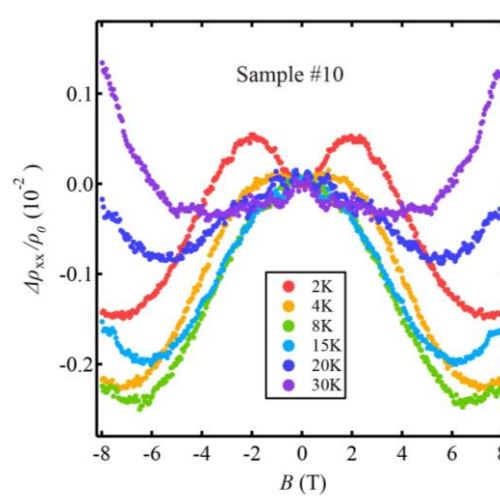
## 5. Gate-tunable negative longitudinal MR of sample #3 with $I//b$



**Figure S5 | Negative longitudinal MR of sample #3 for various  $V_{bg}$ .** The extracted  $C_w$  data are plotted in the inset of Fig. 3b in the main text.

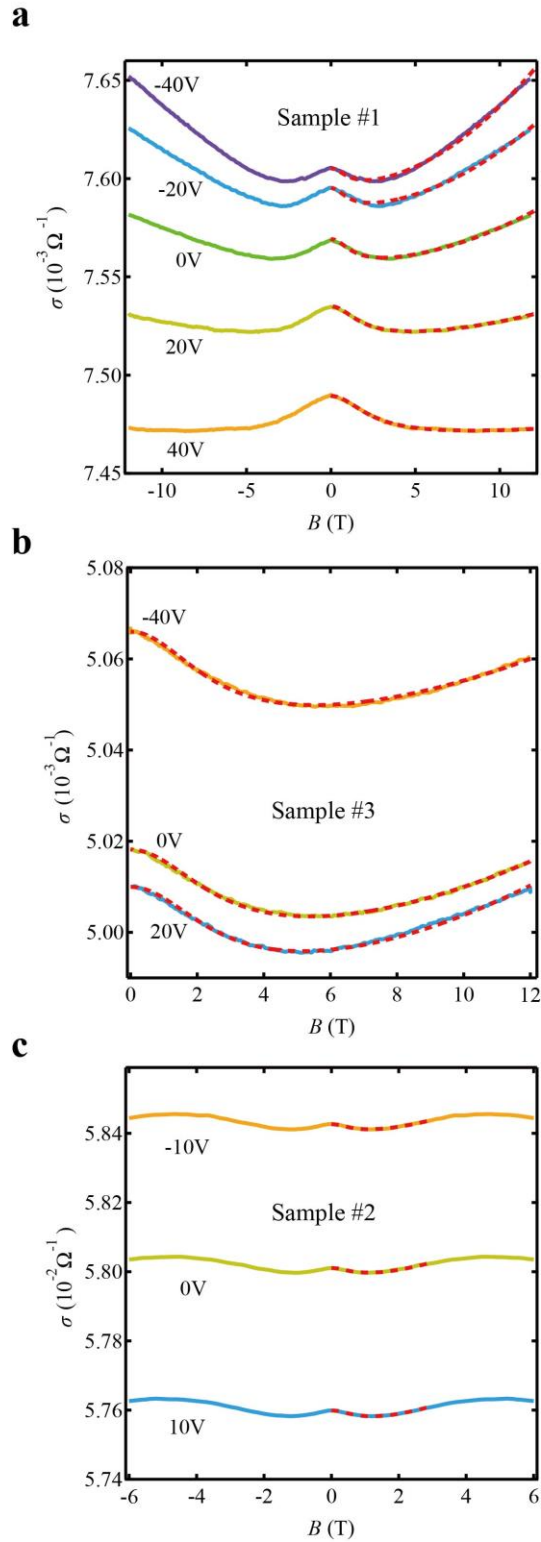
## 6. Temperature dependence of the negative longitudinal MR

Fig. S6 shows the measured negative longitudinal MR of sample #10 at different temperatures. The WAL effect almost disappears at 8 K, while the negative longitudinal MR persists at much higher temperature (up to 30 K), indicating that the negative longitudinal MR is less temperature-sensitive than the WAL effect.



**Figure S6 | Negative longitudinal MR of sample #10 measured at different temperatures with  $B//I//b$ .**

## 7. Semi-classical fitting results of the gate-dependent negative longitudinal MR



**Figure S7 | Fitting results of different samples at different  $V_{bg}$ .** The solid lines and red dashed lines are the experimental and fitting curves, respectively.

To quantitatively analyze the back-gate-tunable negative longitudinal MR, we used the semi-classical formula Eq. (2) to extract the chiral coefficient  $C_w$  as described in the main text. Fig. S7 shows the fitting results and experimental curves of samples #1, #3 and #2. For sample #2, because of the contribution of positive longitudinal MR at high magnetic fields, we only fitted the negative longitudinal region (0-3 T).

## 8. Landau level index of SDH oscillation

We calculated the Landau level index of various samples by analyzing the SDH oscillation data. The Landau level index can be obtained from the Onsager relation:

$$S_F(B) = \frac{2\pi e B}{\hbar} (N + \gamma)$$

where  $S_F = 2\pi e F/\hbar$ , and  $F$  is the frequency of the SDH oscillations. Fig. S8 shows the SDH oscillation data of sample #4. Because of the complete Fermi surface and sample-dependent Fermi energy, the obtained frequencies are different for various samples. Here, we calculated the Landau levels of three samples with an applied magnetic field of approximately 11 T. The corresponding frequencies and Landau level indexes are shown in Table S1.



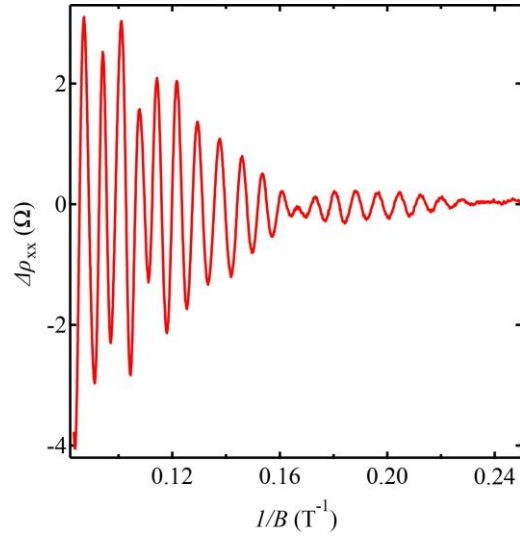


**Figure S8 | SDH oscillation data of sample #4.**

Sample	Landau level Index N	F(T)
sample #1	10	112.92
sample #2	11	122.07
sample #4	14	149.54

**Table S1 | Landau level index of three samples exhibiting negative longitudinal MR.**

## 9. Theoretical calculation of the band structure and the anisotropy of chiral anomaly of WTe<sub>2</sub>

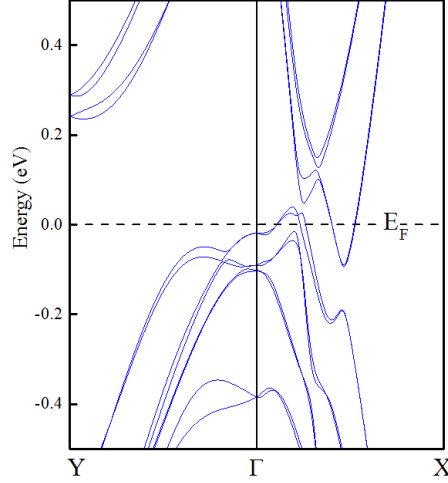


**Figure S9 | Band structure of WTe<sub>2</sub> along the Y-Γ-X direction with SOC.**

As presented in Nature 527, 495-498 (2015): “The chiral anomaly appears in a WP2 only when the direction of the magnetic field is within a cone where  $|T(\mathbf{k})| > |U(\mathbf{k})|$ . If the field direction is outside this cone, then the Landau-level spectrum is gapped and has no chiral zero mode.”

Owing to the  $C_{2T}$  symmetry, we can get the general form of the Hamiltonian around a Weyl point while keeping only terms linear with  $\mathbf{k}$

$$H(\mathbf{k}) = Ak_x + Bk_y + (ak_x + bk_y)\sigma_y + (ck_x + dk_y)\sigma_z + ek_z\sigma_x$$

The energy spectrum of  $H(\mathbf{k})$  can be expressed as

$$\varepsilon_{\pm}(\mathbf{k}) = Ak_x + Bk_y \pm \sqrt{(ak_x + bk_y)^2 + (ck_x + dk_y)^2 + (ek_z)^2}$$

Hence the kinetic and potential components can be expressed as

$$T(\mathbf{k}) = Ak_x + Bk_y, U(\mathbf{k}) = \sqrt{(ak_x + bk_y)^2 + (ck_x + dk_y)^2 + (ek_z)^2}$$

We can thus define the ratio around the Weyl point

$$R = (T(\mathbf{k}))^2 / (U(\mathbf{k}))^2 = \frac{(Ak_x + Bk_y)^2}{(ak_x + bk_y)^2 + (ck_x + dk_y)^2 + (ek_z)^2}$$

While the direction of  $R > 1$  permits the existence of chiral anomaly, we calculated the values of  $R$  along  $\mathbf{a}$  and  $\mathbf{b}$  axes. For the Weyl points at  $E=52\text{meV}$  with respect to the Fermi level, we can get  $R=0.57$  along  $\mathbf{a}$  direction while  $R=143.68$  along  $\mathbf{b}$  direction. For the other four Weyl points at  $E=58\text{meV}$ ,  $R=0.63$  along  $\mathbf{a}$  direction while  $R=9.3$  along  $\mathbf{b}$  direction. The calculated results predict the absence of the chiral anomaly along the direction of  $\mathbf{a}$  axis, and the existence of chiral anomaly along the direction of  $\mathbf{b}$  axis for all Weyl points, which agree well with our observations in experiments.

## References:

1. Kong, W. D. *et al.*, Raman scattering investigation of large positive magnetoresistance material  $\text{WTe}_2$ . *Appl. Phys. Lett.* **106**, 081906 (2015).
2. Soluyanov, A. A. *et al.*, Type-II Weyl semimetals. *Nature* **527**, 495-498 (2015).